Short communication

Preparation and supercapacitance of CuO nanosheet arrays grown on nickel foam

Guiling Wang, Jichun Huang, Shuli Chen, Yinyi Gao, Dianxue Cao*

Key Laboratory of Superlight Material and Surface Technology of Ministry of Education, College of Material Science and Chemical Engineering, Harbin Engineering University, Natong St #145, Harbin 150001, PR China

A B S T R A C T

CuO nanosheet arrays freely standing on nickel foam are prepared via a template-free growth method. The morphology of CuO nanosheet arrays is examined by scanning and transmission electron microscopy and the phase structure of nanosheets is analyzed by X-ray diffraction spectroscopy. The supercapacitance of CuO nanosheet arrays is investigated by cyclic voltammetry, galvanostatic charge/discharge test and electrochemical impedance spectroscopy. The results show that the array of CuO nanosheets forms a uniform film of around 5 μm in thickness on nickel foam skeleton. The film is composed of clusters of arrays of nanosheets with a thickness up to around 150 nm. The CuO nanosheet arrays exhibit a specific capacitance of 569 F g^{-1} at a current density of 5 mA cm^{-2} in 6.0 mol dm^{-3} KOH electrolyte. The capacitance loss is less than 17.5% after 500 charge/discharge cycles at 10 mA cm^{-2} and with columbic efficiency higher than 93%.

© 2011 Elsevier B.V. All rights reserved.

1. Introduction

Electrochemical capacitors (supercapacitors) have higher power density, longer charge/discharge cycle life, higher energy efficiency, but lower energy density than batteries. They can complement batteries in electrical energy storage and harvesting applications when high power delivery or uptake is needed. For example, the combined system of supercapacitors and rechargeable batteries or fuel cells is considered to be the promising power source for pure electric vehicles, in which supercapacitors supply the necessary high power for acceleration and allow for recapture of brake energy, while batteries provide the energy for long distance running [1–5]. Therefore, the development of high performance and low cost electrode materials for supercapacitors has attracted increased interest in recent years. Three major types of electrode materials are reported: carbon (e.g. activated carbon, carbon nanotuble, graphene) for electrochemical double layer capacitors; metal oxides (e.g. RuO$_2$, MnO$_2$, Fe$_3$O$_4$, Co$_3$O$_4$, NiO, SnO$_2$, and V$_2$O$_5$); and conducting polymers (e.g. polyaniline, polypyrrole) for pseudo-capacitors [3,4].

CuO has attractive features like low cost, abundant resources, non-toxicity, and easy preparation in diverse shapes of nano-sized dimension, such as nanospheres, nanoflowers, nanorods, and nanotubes. It has been widely investigated as electrode material for rechargeable Li-ion batteries [6–13]. A strong dependence of specific capacity for Li$^+$ storage on the shape and structure of the nano-sized CuO was demonstrated.

Recently, the supercapacitance behavior of CuO has attracted research interest [14–17]. Zhang et al. reported that CuO with flower-like nanostructures displayed a specific capacitance of 133.6 F g^{-1} in KOH electrolyte, which is about threefold higher than commercial CuO powder [16,17]. Lokhande et al. prepared a thin film of CuO multilayer nanosheets, which showed a specific capacitance of 43 F g^{-1} in Na$_2$SO$_4$ electrolyte [14,15]. Although studies have indicated that CuO is a potential electrode material for supercapacitors, the specific capacitance of CuO is still much lower than other transition metal oxides, such as 1300 and 2200 F g^{-1} for MnO$_2$ and Co$_3$O$_4$, respectively [18,19].

In this study, CuO nanosheet arrays were directly grown onto nickel foam via a simple template-free method to obtain a conducting additive-free and binderless electrode with high utilization of the active material. CuO nanosheet arrays exhibited higher specific capacitance than reported in the literature.

2. Experimental

The electrode of CuO nanosheet arrays on nickel foam was prepared via a template-free growth method. A growth solution was prepared by dissolving 2.5 mmol Cu(NO$_3$)$_2$ and 1.25 mmol NH$_4$NO$_3$ in 4.5 cm^3 ammonia (25 wt%) + 9 cm^3 H$_2$O. The solution was magnetically stirred for 10 min in air at room temperature and heated at 90 ± 1 °C for 2 h in an oven. A piece of nickel foam (10 mm × 10 mm × 1.1 mm, 110 PPI, 320 g m^{-2}, Changsha Lyrun

* Corresponding author. Tel.: +86 51 82589036; fax: +86 451 82589036.
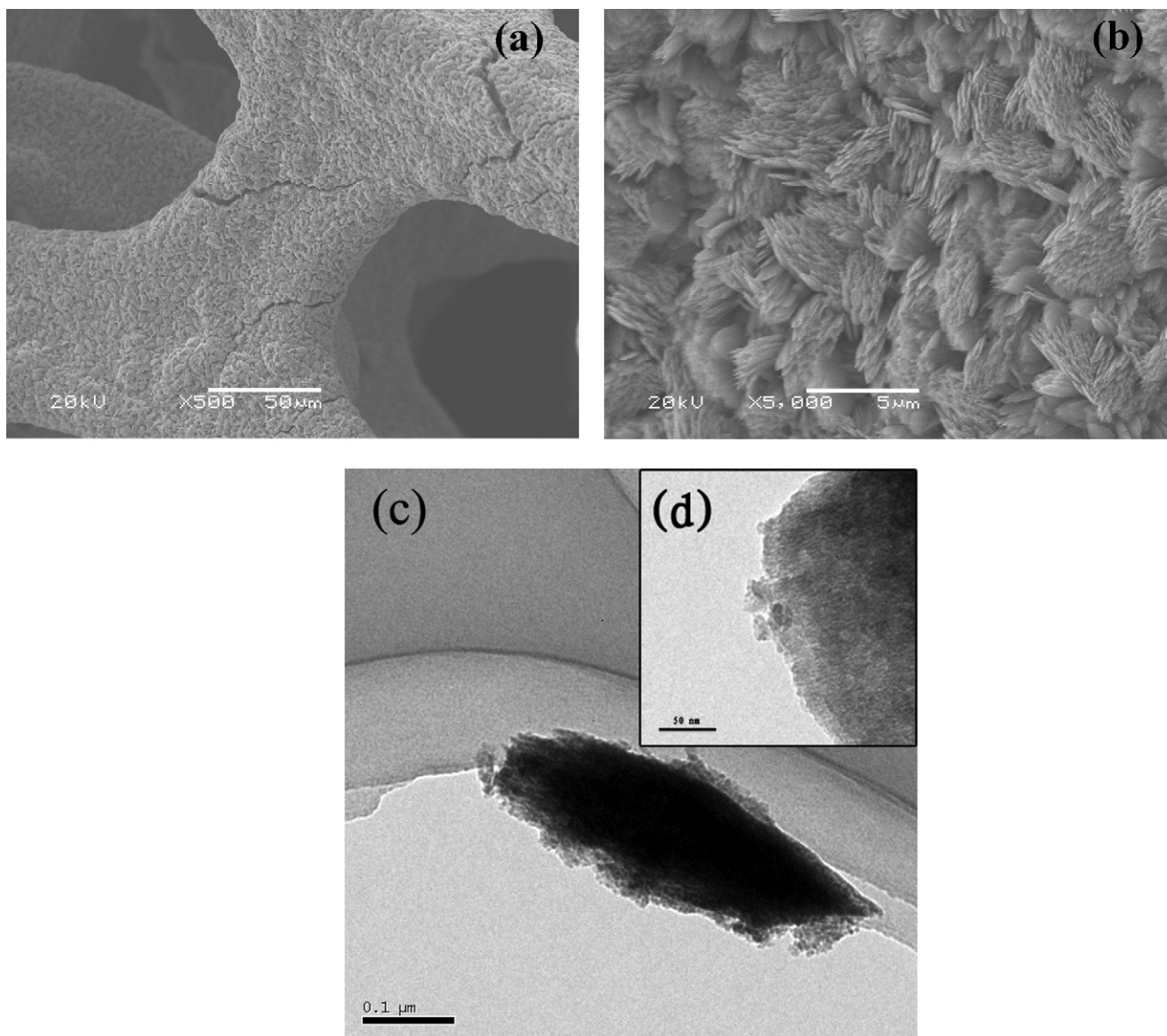*E-mail address:* caodianxue@hrbeu.edu.cn (D. Cao).

Fig. 1. The SEM images of the NSA-CuO/Ni-foam electrode (a and b) and the TEM images of a single CuO nanosheet scratched down from the nickel foam (c and d).

Material Co., Ltd. China) was pretreated by degreasing in acetone, etching in $6.0 \, mol \, dm^{-3}$ HCl for 15 min, rinsing with water, soaking in $0.1 \, mmol \, dm^{-3}$ $NiCl_2$ for 4 h, and rinsing again thoroughly with water. The pretreated nickel foam substrate was then hung in the growth solution for 6 h at $90 \pm 1 \,°C$ to allow the growth of CuO array of nanosheets. After growth, the electrode was washed with water and heated at $90 \pm 1 \,°C$ for 0.5 h to obtain the final electrode (denoted as NSA-CuO/Ni-foam, NSA represents NanoSheet Arrays), containing 7 mg CuO. The morphology of CuO array of nanosheets was examined by scanning electron microscope (SEM, JEOL JSM-6480) and transmission electron microscope (TEM, FEI Teccai G2 S-Twin, Philips). The structure of the nanosheets was analyzed using X-ray diffractometer (XRD, Rigaku TTR III) with Cu K_α radiation ($\lambda = 0.1506 \, nm$). The 2θ ranged from $10°$ to $90°$ with a scan rate of $10° \, min^{-1}$ and a step width of $0.02°$.

Electrochemical measurements were performed in a conventional three-electrode electrochemical cell using a computerized potentiostat (Autolab PGSTAT302, Eco Chemie) controlled by Nova software. The prepared electrode ($1 \, cm^2$ nominal planar area) acted as working electrode, a platinum foil ($1 \, cm \times 2 \, cm$) served as counter electrode, and a saturated calomel electrode (SCE) was used as reference electrode. All potentials were referred to the reference electrode and all electrochemical measurements were performed at room temperature in aqueous KOH solution. All solutions were made with analytical grade chemical reagents and Millipore Milli-Q water ($18 \, M\Omega \, cm$). Electrochemical impedance spectroscopy (EIS) measurements were carried out by applying an AC voltage with 5 mV amplitude in a frequency range from 0.01 Hz to 100 kHz at the open circuit potential.

3. Results and discussion

3.1. Characterization of the NSA-CuO/Ni-foam electrode

Fig. 1 shows the SEM images of the CuO nanosheet arrays attached onto nickel foam skeleton and the TEM images of a single CuO nanosheet scratched down from the nickel foam. The SEM image at low magnification (Fig. 1a) shows that CuO forms a thick, uniform film, which completely covers the nickel foam skeleton. A few cracks are identified as having formed during thermal treatment after growth. The thickness of the film, determined from the depth of the cracks, is around 5 μm. The SEM image at high magni-

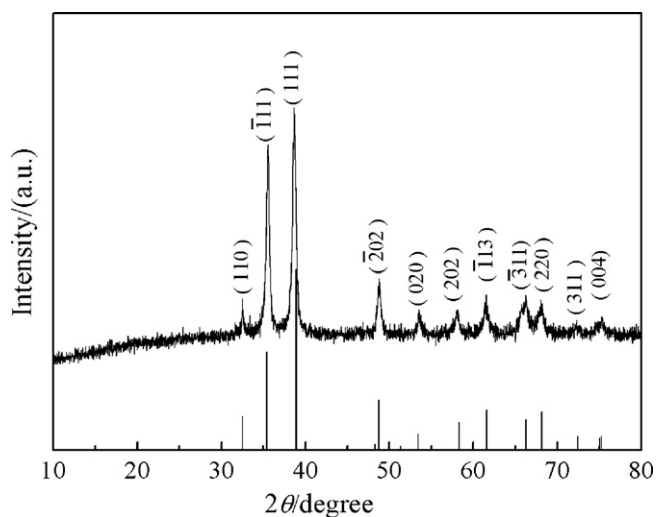**Fig. 2.** XRD patterns of CuO nanosheets scratched down from the nickel foam.

Fig. 3. Cyclic voltammograms of the NSA-CuO/Ni-foam electrode in different concentration KOH electrolytes at a scan rate of 5 mV s^{-1}.

fication (Fig. 1b) indicates that the film is composed of clusters of parallel packed arrays of nanosheets, of which the majority orientate almost vertically to the nickel foam substrate. The thickness of a single nanosheet is up to around 150 nm. TEM images (Fig. 1c and d) further confirm the nanosheet shape and show that the nanosheets are composed of interconnected CuO nanoparticles with diameters of around 5 nm. The inner pores within each nanosheet and the interspaces between neighboring nanosheets will allow easy diffusion of the electrolyte into the nanosheet matrix to provide the electrode with a large electrochemical active area.

Fig. 2 shows the XRD patterns of the powder sample scratched from nickel foam. All the diffraction peaks of the sample match well with the standard XRD pattern of monoclinic CuO (JCPDS card No. 05-0661), and without peaks arising from impurity, such as Cu_2O and $Cu(OH)_2$. The lattice constants were calculated to be $a = 0.4688$ nm; $b = 0.3421$ nm, $c = 0.5135$ nm and $\beta = 99.30°$ for the sample; they are consistent with the standard values of CuO ($a = 0.4684$ nm, $b = 0.3425$ nm, $c = 0.5129$ nm and $\beta = 99.49°$). The sample can, therefore, be identified as pure phase monoclinic CuO. The broadened diffraction peaks indicate the small crystallite size of the sample, which is around 24 nm, estimated using Scherrer's relationship based on the half width of the [1 1 1] peak.

3.2. Supercapacitance performance of the NSA-CuO/Ni-foam electrode

Fig. 3 shows the typical stabilized cyclic voltammograms (CVs) of the NSA-CuO/Ni-foam electrode in different concentrations of KOH electrolyte. Obvious anodic and cathodic peaks are observed in the potential range of −0.2 to 0.6 V, indicating that the NSA-CuO/Ni-foam electrode possesses pseudocapacitance properties. The concentration of KOH has a significant effect on the profile of the CVs. At KOH concentration below 1.0 mol dm^{-3}, the CV displays a well resolved anodic peak at around 0.4 V (A_1). This peak becomes broader when the KOH concentration increases to 3.0 mol dm^{-3}. With a further increase in KOH concentration, the broad anodic peak splits into two peaks (A_1 and A_2) and the peak potential shifts to a lower potential. The charges corresponding to the anodic peaks increase with an increase of KOH concentration up to 0.6 mol dm^{-3}, but decreases with further increase to 8.0 mol dm^{-3}. The onset potential for oxygen evolution reaction shifts to a more negative potential at 8.0 mol dm^{-3} KOH. At all KOH concentrations, two cathodic peaks (C_1 and C_2) are observed, the one at higher potential is relatively well-developed and sharp, and the other at lower
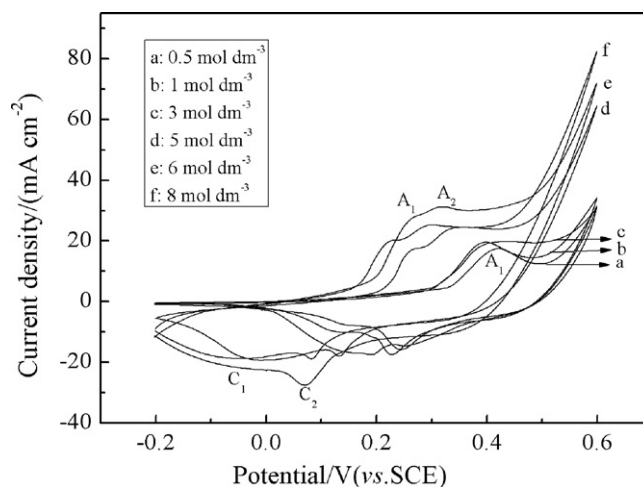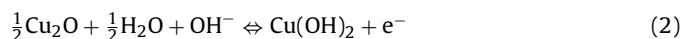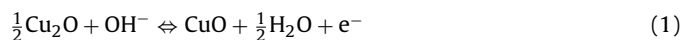
potential is broader. The charges corresponding to cathodic peaks increase with increase of KOH concentration up to 0.6 mol dm^{-3}. These results show that higher specific capacitance can be obtained at higher KOH concentration with an upper of limit of 0.6 mol dm^{-3}.

The CV of CuO in NaOH is quite complex with differences in the literature about the assignment of the anodic and cathodic peaks. Based on literature reports about CV of CuO in alkaline electrolytes [20–26], the following redox reactions may be involved in the transition between Cu(I) and Cu(II) species.

$$\tfrac{1}{2}Cu_2O + OH^- \Leftrightarrow CuO + \tfrac{1}{2}H_2O + e^- \tag{1}$$

$$\tfrac{1}{2}Cu_2O + \tfrac{1}{2}H_2O + OH^- \Leftrightarrow Cu(OH)_2 + e^- \tag{2}$$

$$CuOH + OH^- \Leftrightarrow CuO + H_2O + e^- \tag{3}$$

$$CuOH + OH^- \Leftrightarrow Cu(OH)_2 + e^- \tag{4}$$

The peak A_1 appearing at both low and high KOH concentration can be attributed to the oxidation of Cu_2O (or CuOH) to CuO (Eq. (1) and/or (3)). The peak A_2 occurring only at high KOH concentration may be due to the oxidation of Cu_2O (or CuOH) to both CuO and $Cu(OH)_2$ (Eqs. (1)–(4)) [20,21,24–26]. The cathodic peaks C_1 and C_2 can be ascribed to the reduction of CuO (Eq. (1) and/or (3)) and the reduction of $Cu(OH)_2$ (Eq. (2) and/or (4)), respectively, according to the literature [20,21,24–26]. However, further investigation is required to identify the peak assignments. The reduction of CuO to Cu and the oxidation of CuO to Cu(III) species (such as Cu_2O_3) are unlikely to occur in the potential range of this study [23,27]. Nevertheless, it can be concluded that the capacitance of CuO originates from the redox reaction of Cu(I)/Cu(II) couple. It should be pointed out that the CVs shown in Fig. 3 are the stabilized curves after around 5 potential cycles, during which CuO originally formed on nickel foam was partially reduced to Cu_2O. The oxidation of this Cu_2O generated the first anodic peak (A_1).

Fig. 4 shows the CVs of the NSA-CuO/Ni-foam electrode recorded in 6.0 mol dm^{-3} KOH solution at different scan rates. With the increase of scan rate (v), the anodic peaks shift toward the positive potential and cathodic peaks shift toward the negative potential, demonstrating the quasi-reversible nature of the redox reactions. The two anodic peaks merge, and likewise the two cathodic peaks, at high scan rates to a single broad anodic and cathodic peak, respectively. The plots of peak currents (i_p) against $v^{1/2}$ show a nearly linear relationship, implying the electrode reactions are diffusion-controlled with electrolyte involved (Eqs. (1)–(4)). To avoid the occurrence of oxygen evolution reaction during the charge process, the upper limit potential should be less than
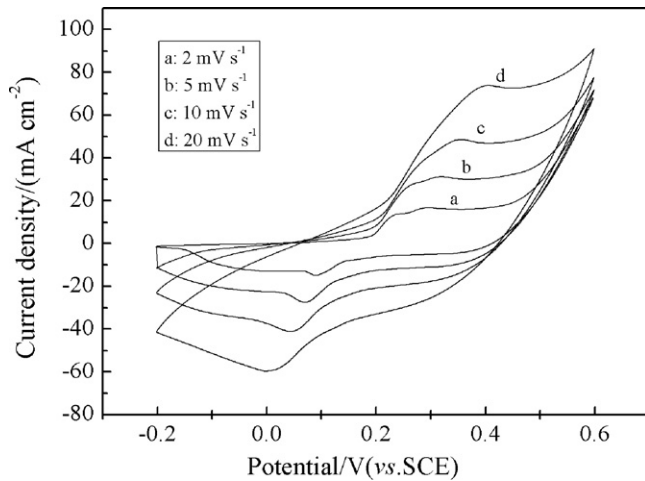
Fig. 4. Cyclic voltammograms of the NSA-CuO/Ni-foam electrode in 6.0 mol dm^{-3} KOH solution at different scan rates between 2 and 20 mV s^{-1}.

Fig. 6. The discharge curves of the NSA-CuO/Ni-foam electrode at different current densities in 6.0 mol dm^{-3} KOH solution.
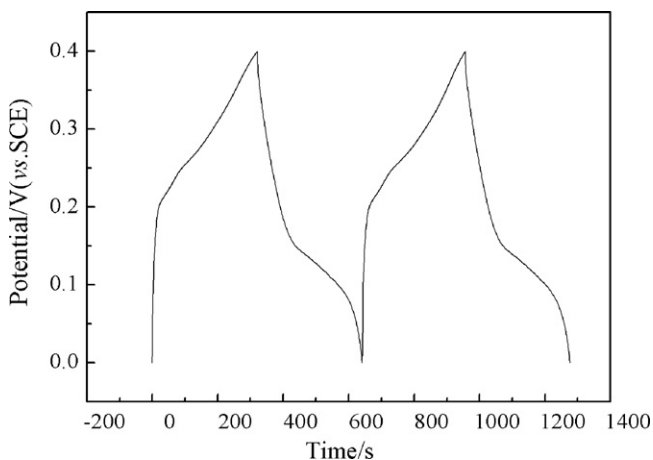
0.4 V. Fig. 5 shows the first and second charge/discharge curves of the NSA-CuO/Ni-foam electrode in 6.0 mol dm^{-3} KOH solution at a galvanostatic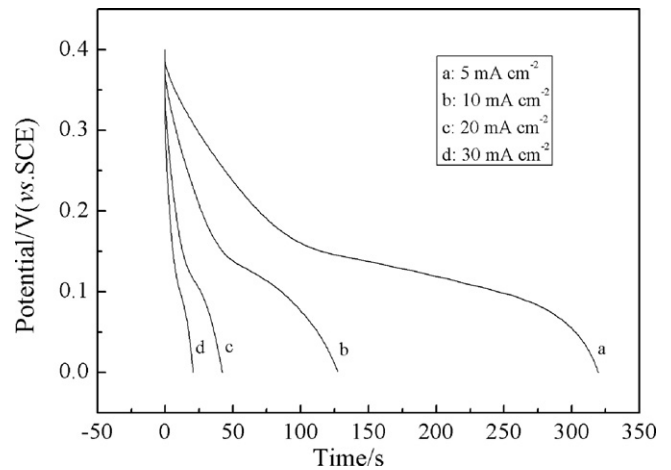 current density of 5 mA cm^{-2} (corresponding to 0.714 A g^{-1}) in the potential range of 0–0.4 V. The charge curves indicate that most of the capacitance is generated in the potential range of 0.2–0.4 V, corresponding to the oxidation reaction of Cu(I) to Cu(II), as demonstrated in the CVs. The discharge curve consists of two sections, a fast potential drop followed by a slow potential decay. Each section accounts for about half of the total specific capacitance. The two sections may correspond to reduction of CuO and Cu(OH)$_2$ to Cu(I) species according to the CVs and the literature [24]. Since CuO is thermodynamically more stable than Cu(OH)$_2$ at high pH [26], Cu(OH)$_2$ is likely to be discharged first. The obvious non-linear shape of the discharge curves (Fig. 5) and the non-ideal rectangular shape of the CV (Figs. 3 and 4) reveal that the capacitance of the NSA-CuO/Ni-foam electrode mainly originates from faradic reactions, instead of double-layer charge and discharge.

Fig. 6 shows the influence of discharge current density on the specific capacity of the NSA-CuO/Ni-foam electrode. The specific capacitance was calculated according to the following equation:

$$C_m = \frac{I_d \times \Delta t}{\Delta V \times m} \tag{5}$$

where C_m (F g^{-1}) is the specific capacitance, I_d (mA) is the discharge current, Δt (s) is the discharge time, ΔV (V) is the discharge

potential range, and m (mg) is the mass of CuO (7 mg). The specific capacitance values of the CuO evaluated from the discharge curves are 569, 454, 301, and 221 F g^{-1} at the current density of 5, 10, 20, and 30 mA cm^{-2}, respectively. The specific capacitance of our CuO nanosheet arrays is much higher than that of other forms of CuO reported in the literature, i.e. Zhang et al. [16,17] reported a specific capacitance of 133.6 F g^{-1} (in KOH electrolyte at a current density of 10 mA cm^{-2}) for flower-like monoclinic CuO, and Lokhande et al. [14,15] reported a specific capacitance of 43 F g^{-1} (in Na$_2$SO$_4$ electrolyte at a scan rate of 10 mV s^{-1}) for amorphous CuO thin films of multilayer nanosheets. The large capacitance of our CuO nanosheet arrays can be attributed to the unique porous nanostructure and the high utilization of active material. The significant capacitance decrease resulting from the increase of discharge current density is likely caused by the increase of potential drop due to electrode resistance and the relatively insufficient Faradic redox reaction of CuO under higher discharge current densities. The ohmic resistance of the NSA-CuO/Ni-foam electrode is 3 Ω cm^2 calculated from the initial sudden potential drop, which leads to a potential decay of 15 mV at 5 mA cm^{-2} and 90 mV at 30 mA cm^{-2}. This large ohmic resistance can be attributed to the formation of Cu$_2$O, a poor conducting semiconductor [25].

The cycling stability and the columbic efficiency of the NSA-CuO/Ni-foam electrode are shown in Fig. 7. The columbic efficiency
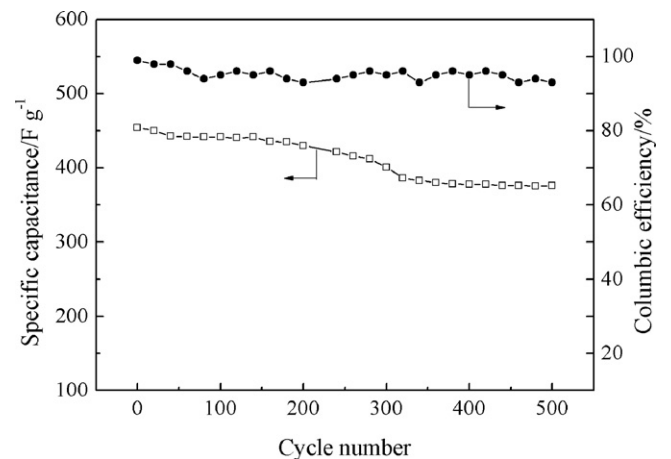

Fig. 5. The first and second charge/discharge curves of the NSA-CuO/Ni-foam electrode in 6.0 mol dm^{-3} KOH solution at a galvanostatic current density of 5 mA cm^{-2}.

Fig. 7. Dependences of the discharge specific capacitance and the columbic efficiency on the charge/discharge cycle numbers. The charge/discharge tests were performed at 10 mA cm^{-2} in 6.0 mol dm^{-3} KOH solution.
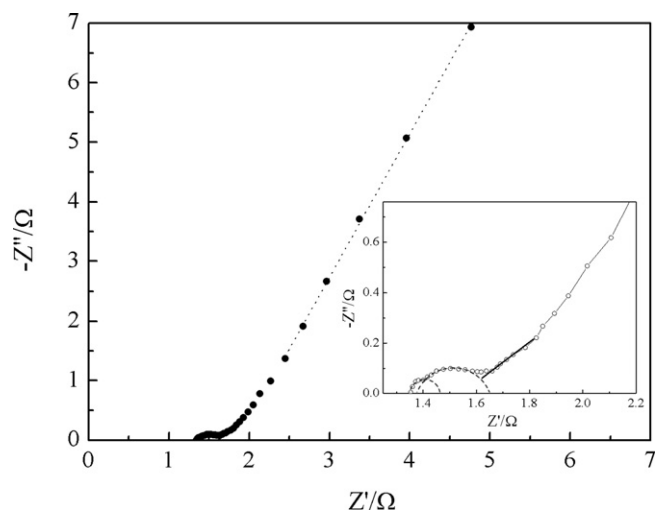
Fig. 8. The electrochemical impedance spectrum of the NSA-CuO/Ni-foam electrode in 6.0 mol dm^{-3} KOH at open circuit potential.

was calculated using the following equation:

$$\eta = \frac{t_d}{t_c} \times 100 \qquad (6)$$

where t_c and t_d represent the time of charge and discharge, respectively. In the first 350 cycles, the discharge specific capacitance gradually decreases from 454 to 380 F g^{-1} corresponding to a capacitance loss of 16%. After 350 cycles, the specific capacity stabilizes at about 375 F g^{-1}. The columbic efficiency remains above 93% within 500 cycles. The repetitive charge/discharge cycling does not induce noticeable changes of the structural array of CuO nanosheets and the peeling off of CuO from nickel foam does not occur. Reasons responsible for the capacitance decrease are under investigation, and may involve microstructure change, active surface area loss and resistance increase.

EIS of the NSA-CuO/Ni-foam electrode was measured at open circuit potential in 6.0 mol dm^{-3} KOH solution and the Nyquist plot is shown in Fig. 8. The spectrum exhibits two partially intercrossed and depressed semicircles at the high frequency region, which can be ascribed to the redox reactions between Cu(I) and Cu(II) species. The depression of the semicircles is an indication of surface roughness of the electrode. The low frequency region consists of two straight lines: the first, a 52° straight line at the higher frequency region corresponds to Warburg impedance related to the diffusion of electrolyte within the pores of the electrode; the second, a 62° straight line at the lower frequency region demonstrates the capacitance nature of the electrode (vertical line for an ideal capacitor). The EIS results show the pseudo-capacitance characteristics and the porous structure feature of the NSA-CuO/Ni-foam electrode.

4. Conclusions

CuO nanosheet arrays were successfully grown onto nickel foam by a one-step template-free method to obtain a conduct-ing additive-free and binderless electrode for supercapacitors. The nanosheets, with near vertical orientation on nickel foam substrate, are composed of interconnected nanoparticles. The unique structure of the electrode CuO has high utilization and superior properties for electrolyte diffusion. The CuO exhibits the highest reported specific capacitance of 569 F g^{-1} at a current density of 5 mA cm^{-2}. Electrolyte concentration exerts a significant effect on the performance of CuO capacitance. Considering low cost, abundance resources and high specific capacitance, CuO has a promising future as potential electrode material for pseudo-supercapacitors.

References

[1] A. Burke, J. Power Sources 91 (2000) 37–50.
[2] R. Kotz, M. Carlen, Electrochim. Acta 45 (2000) 2483–2498.
[3] P. Simon, Y. Gogotsi, Mater. Nat. 7 (2008) 845–854.
[4] Y. Zhang, H. Feng, X. Wu, L. Wang, A. Zhang, T. Xia, H. Dong, X. Li, L. Zhang, Int. J. Hydrogen Energy 34 (2009) 4889–4899.
[5] A. Burke, Electrochim. Acta 53 (2007) 1083–1091.
[6] J.Y. Xiang, J.P. Tu, L. Zhang, Y. Zhou, X.L. Wang, S.J. Shi, J. Power Sources 195 (2010) 313–319.
[7] J.Y. Xiang, J.P. Tu, L. Zhang, Y. Zhou, X.L. Wang, S.J. Shi, Electrochim. Acta 55 (2010) 1820–1824.
[8] J.Y. Xiang, J.P. Tu, J. Zhang, J. Zhong, D. Zhang, J.P. Cheng, Electrochem. Commun. 12 (2010) 1103–1107.
[9] S. Grugeon, S. Laruelle, R. Herrera-Urbina, L. Dupont, P. Poizot, J.M. Tarascon, J. Electrochem. Soc. 148 (2001) A285–A292.
[10] X.P. Gao, J.L. Bao, G.L. Pan, H.Y. Zhu, P.X. Huang, F. Wu, D.Y. Song, J. Phys. Chem. B 108 (2004) 5547–5551.
[11] L.B. Chen, N. Lu, C.M. Xu, H.C. Yu, T.H. Wang, Electrochim. Acta 54 (2009) 4198–4201.
[12] Q. Pan, H. Jin, H. Wang, G. Yin, Electrochim. Acta 53 (2007) 951–956.
[13] F.S. Ke, L. Huang, G.Z. Wei, L.J. Xue, J.T. Li, B. Zhang, S.R. Chen, X.Y. Fan, S.G. Sun, Electrochim. Acta 54 (2009) 5825–5829.
[14] D.P. Dubal, D.S. Dhawale, R.R. Salunkhe, V.S. Jamdade, C.D. Lokhande, J. Alloys Compd. 492 (2010) 26–30.
[15] V.D. Patake, S.S. Joshi, C.D. Lokhande, O.S. Joo, Mater. Chem. Phys. 114 (2009) 6–9.
[16] H. Zhang, M. Zhang, Mater. Chem. Phys. 108 (2008) 184–187.
[17] H. Zhang, J. Feng, M. Zhang, Mater. Res. Bull. 43 (2008) 3221–3226.
[18] M. Toupin, T. Brousse, D. Belanger, Chem. Mater. 16 (2004) 3184–3190.
[19] M.J. Deng, F.L. Huang, I.W. Sun, W.T. Tsai, J.K. Chang, Nanotechnology 20 (2009) 175602 (5 pp.).
[20] M. Kang, A.A. Gewirth, J. Phys. Chem. B 106 (2002) 12211–12220.
[21] M. Jayalakshmi, K. Balasubramanian, J. Electrochem. Sci. Int. 3 (2008) 1277–1287.
[22] S. Komorsky-Lovric, L. Marinic-Pajc, N. Tadej, A.J.M. Horvat, J. Petran, J. Electroanal. Chem. 623 (2008) 75–80.
[23] S. Nakayama, A. Kimura, M. Shibata, S. Kuwabata, T. Osakai, J. Electrochem. Soc. 148 (2001) B467–B472.
[24] J.B. He, D.Y. Lu, G.P. Jin, Appl. Surf. Sci. 253 (2006) 689–697.
[25] L.D. Burke, M.J.G. Ahern, T.G. Ryan, J. Electrochem. Soc. 137 (1990) 553–561.
[26] G.M. Brisard, J.D. Rudnicki, F. McLarnon, E.J. Cairns, Electrochim. Acta 40 (1995) 859–865.
[27] S.M. Abd el Haleem, B.G. Ateya, J. Electroanal. Chem. 117 (1981) 309–319.